



### **Science Arts & Métiers (SAM)**

is an open access repository that collects the work of Arts et Métiers Institute of Technology researchers and makes it freely available over the web where possible.

This is an author-deposited version published in: <https://sam.ensam.eu>  
Handle ID: <http://hdl.handle.net/10985/23922>

#### **To cite this version :**

Martin BOURHIS, Michaël PEREIRA, Florent RAVELET - Experimental investigation of the effects of the Reynolds number on the performance and near wake of a wind turbine - Renewable Energy - Vol. 209, p.63-70 - 2023

Any correspondence concerning this service should be sent to the repository

Administrator : [scienceouverte@ensam.eu](mailto:scienceouverte@ensam.eu)



# Experimental investigation of the effects of the Reynolds number on the performance and near wake of a wind turbine

M. Bourhis<sup>a,\*</sup>, M. Pereira<sup>a</sup>, F. Ravelet<sup>a</sup>

<sup>a</sup>*Arts et Metiers Institute of Technology, CNAM, LIFSE, HESAM University, 75013 Paris, France*

---

## Abstract

Wind tunnel experiments provide worthwhile insights for designing efficient micro wind energy harvesters and large-scale wind turbines. As wind tunnel tests with large-scale wind turbines are expensive and not always feasible, most experiments are conducted with geometrically scaled rotors. Furthermore, micro-scale runners used for wind energy harvesting face the issue of lower efficiency than large turbines. A better understanding of Reynolds number effects induced by the downsizing of a turbine would help to design more efficient wind energy harvesters and more faithfully scaled experiments. This paper reports on Reynolds number effects on the performance and wake of micro-scale wind turbines. Wind turbines' power and torque coefficients are measured in a wind tunnel for a wide range of Reynolds numbers. The wake axial velocity fields and the vortex core locations are collected for three Reynolds numbers using phase-averaged and phase-locked stereoscopic particle image velocimetry techniques. The results emphasize that an increase in the Reynolds number leads to larger power coefficients, torque coefficients, and optimum tip-speed ratios. Higher Reynolds numbers induce wider wake expansion and a larger axial velocity defect. This quantitative analysis will contribute to a clearer understanding of the scaling effects and help to design more efficient wind energy harvesters.

*Keywords:* Micro-scale wind turbines, Reynolds number effects, wind energy harvesting, stereoscopic particle image velocimetry, wake analysis

---

## 1. Introduction

Wind energy, as a clean and renewable energy source, is one of the most attractive alternative to high-carbon fossil fuels. Even though wind power is highly intermittent, its potential for electricity production is considerable [1]. From light breezes in urban areas to strong offshore winds, wind energy is readily available everywhere and shows wide variations in strength. In order to capture the abundant wind resources and thus meet the growing domestic energy demand, many wind farms are projected to be built [2]. Furthermore, the energy harvesting of low-speed airflow is of particular interest nowadays to support the fast development of wireless autonomous monitoring sensors in the field of the Internet Of Things (IOT) [3]. Miniature wind energy harvesters, such as micro-scale horizontal axis wind turbines, could collect the energy of low-speed airflow in urban areas [4] to power a rechargeable battery or capacitor of an IOT endpoint [5].

The design of efficient large-scale wind turbines and small rotating energy harvesters require precise knowledge of the effects of the Reynolds number  $Re$  on the performance and wake's characteristics downstream a rotor.

Firstly, large-scale wind turbines are not usually tested in wind tunnels. Consequently, the investigation of large-scale turbines' characteristics is performed with geometrically scaled turbines. As the operating

---

\*corresponding author

Email addresses: martin.bourhis@ensam.eu (M. Bourhis), michaelpereira@ensam.eu (M. Pereira), florent.ravelet@ensam.eu (F. Ravelet)

Reynolds number of large-scale turbines is significantly higher than that achieved in a wind tunnel with scaled rotors, a high understanding of the Reynolds number effects on the wake development, interference effects, and performance is required to provide accurate data for the design of large-scale wind turbines based on scaled experiments.

Secondly, it can be observed from the literature that the downsizing of wind turbines is not straightforward. Runners specifically designed for energy harvesting, as well as scaled turbines, achieve lower efficiencies, *i.e.*, lower maximum power coefficients  $C_{p,max}$  than large-scale turbines. The power coefficient  $C_p$  is defined as the ratio of the mechanical power  $P$  to the available power  $P_a$ :

$$C_p = \frac{P}{P_a} = \frac{\tau\omega}{0.5\rho\pi R_T^2 V_\infty^3} \quad (1)$$

where  $\tau$  is the aerodynamic torque,  $\omega$  is the angular velocity,  $R_T$  is the tip radius of the rotor,  $\rho$  is the air density, and  $V_\infty$  is the freestream wind velocity. A large body of literature highlights that as the rotor radius  $R_T$  decreases, so does the maximum power coefficient  $C_{p,max}$ . Most micro-scale turbines ( $R_T \leq 0.1$  m), whether geometrically scaled or designed for energy harvesting, have a maximum power coefficient of around  $C_{p,max} \leq 0.3$  whereas large scale rotors achieve a  $C_{p,max}$  close to 0.5. This partly explains why micro-scale turbines are still not widely employed to supply autonomous IOT devices.

As the rotor diameter is small and the operating freestream wind velocity is low, micro-scale runners operate mainly in low Reynolds number flow conditions ( $Re \leq 10^5$ ). In this study, the Reynolds number is based on the chord length  $c$  and on the relative velocity  $W$  and reads:

$$Re = \frac{\rho W c}{\eta} \quad (2)$$

where  $\eta$  is dynamic viscosity of air.

The effects of the Reynolds number on the power coefficient  $C_p$ , on the torque coefficient  $C_\tau$  and on the initial wake are barely addressed in the literature. However, it is of particular interest to deeply understand flow behavior around a micro-scale rotor in order either to design more efficient runners or to provide a better understanding of the scaling effects of full-scale turbines. The torque coefficient,  $C_\tau$ , is a dimensionless measure of the torque generated by a rotor and reads :

$$C_\tau = \frac{\tau}{0.5\rho\pi R_T^3 V_\infty^2} \quad (3)$$

McTavish et al. investigated Reynolds number effects on the thrust coefficient and wake expansion downstream 2-bladed and 3-bladed 0.25 m horizontal axis wind turbines that were geometrically scaled from a larger one [6]. They conducted water channel experiments within a specific Reynolds number range  $3620 \leq Re \leq 30100$  based on chord length and blade tip-speed. The authors concluded that the wake expansion and thrust coefficient increase with increasing Reynolds numbers. Finally, they advocated to modify the geometry of scale rotor's airfoil in scaling tests to maintain similar thrust and wake expansion. Burdett et al., in Ref. [7], compared the power coefficient of three geometrically scaled rotors, with diameters of 0.5 m, 0.4 m, and 0.3 m, for various upcoming wind velocities. They reported that larger freestream wind velocities lead to larger maximum power coefficients at a quasi-constant optimum tip-speed ratio. They added that the discrepancy in  $C_p$  between the 0.5 m runner and the others at low freestream wind velocities was likely due to a larger relative rugosity that affected the flow separation. Cunningham et al. performed field tests with a low-solidity, 3.74 m diameter horizontal axis wind turbine [8]. Their results show a significant drop in the wind turbine's power coefficient and an increase in the optimum tip-speed ratio  $\lambda_{opt}$  as Reynolds number decreased. The authors reported that the  $C_p$  vs.  $\lambda$  curves's dependence on Reynolds number was caused by variations in the rotor's aerodynamic lift and drag coefficients with the Reynolds number. Another experimental study carried out by Kadrowski et al. reveals that higher Reynolds numbers allow the turbine to reach higher maximum power coefficients  $C_{p,max}$  but at lower optimum tip-speed ratios  $\lambda_{opt}$  [9]. Similar studies have also been conducted with micro-scale vertical axis wind turbines [10, 11]. In a recent study, Li et al. numerically investigated the Reynolds number effects on the power coefficient and

wake structure of a vertical axis wind turbine [11]. They reported that the Reynolds number mainly affects the power coefficient and the evolution of spanwise vortices at small scales and for  $Re \leq 5 \times 10^5$ . They conclude by recommending the use of horizontal rather than vertical-axis micro-scale wind turbines in low Reynolds number flow conditions. In addition, to date, there is no consensual agreement on the effects of low Reynolds numbers on micro-scale wind turbines' performance and very little available data on their effects on a turbine's near wake.

Wind turbine blades ensure the conversion of the kinetic power of the wind into mechanical power; hence, their geometry is closely linked to the flow patterns and to the rotor's performance. The classical method for designing wind turbine blades is called the Blade Element Momentum Theory. Firstly, once determined a design tip-speed ratio, optimum flow conditions are computed using general momentum theory [12]. The rotor is modelled as an actuator disc in general momentum theory, *i.e.*, a rotor with an infinite number of blades that causes a sudden pressure jump. As the thrust force acting over the rotor is a function of the pressure drop, so is the power coefficient. One limitation of the actuator disc theory is that the physical behavior of the blades is not modeled. Consequently, the optimum flow conditions, *i.e.*, the wake and the performance of a rotor, are theoretically not sensitive to a change in the Reynolds number.

Secondly, the chord length and pitch angle distributions are computed to achieve the thrust force derived from general momentum theory. The classical method is based on 2D lift and drag coefficients obtained from wind tunnel experiments performed in high Reynolds number flow conditions with isolated and non-rotating airfoils. Existing research recognizes the critical role played by the Reynolds number on the flow pattern around an isolated airfoil and its aerodynamic properties. It is well acknowledged that an increase in  $Re$  leads to an increase in the lift coefficient  $C_l$  and stall angle and a decrease in the drag coefficient  $C_d$  [13]. No consensual agreement exists on the variation of the optimum angle of attack, *i.e.*, the angle of attack which produces the higher  $C_l/C_d$  ratio, with the Reynolds number.

In practice, Reynolds number effects observed with isolated airfoils should be taken into account in the design of a geometrically scaled turbine or in the design of an efficient micro-scale turbine for energy harvesting. However, as highlighted by Van Treuren et al. in Ref. [14], the available data on 2D airfoils, mainly based on computational tools such as XFOIL, are not robust under the low Reynolds numbers found with micro-scale turbines. Moreover, to meet a nearly similar maximum power coefficient as large-scale runners, micro-scale rotors require a lower optimum tip-speed ratio and a higher blade solidity [15–18]. It induces a mutual interaction between blades that makes the available findings on isolated airfoils useless for the design of either a wind energy harvester or a geometrically scaled turbine [19, 20].

The current experimental study serves two purposes. Firstly, to evaluate the effects of the Reynolds number on the power coefficient  $C_p$  and torque coefficient  $C_\tau$  vs. tip-speed ratio  $\lambda$  curves of a micro-scale wind turbine. To accomplish this, a 300 mm horizontal axis wind turbine, designed specifically for energy harvesting, was scaled down to 200 mm and 100 mm in diameter, respectively. All three runners' characteristics were collected in a wind tunnel for several freestream wind speeds and compared to each other. Secondly, to investigate the initial wake expansion and axial flow velocity defect downstream the 200 mm rotor for three upcoming freestream wind velocities using stereoscopic particle image velocimetry (SPIV).

## 2. Design of the turbines

As noticed in the introduction, wind turbines obtained by applying a geometric factor to large-scale runners achieve low dimensionless performance. Thus, in the current study, the investigation of Reynolds number effects is performed with micro-scale turbines specifically designed for energy harvesting. In other words, they achieve a high level of performance in low Reynolds number flow conditions.

Three high-solidity and low tip-speed ratio runners with diameters equal to 300 mm, 200 mm and 100 mm and identical relative geometries were designed. All turbines' dimensionless parameters are equal in order to get a pure geometrical scaling. The design procedure of the 300 mm runner has been the subject of a preliminary study [15], hence only some relevant design steps are documented in this paper. As reported in Ref. [15], this runner achieves a high maximum power coefficient at its design tip-speed ratio

$C_{p,max}(\lambda = 1) = 0.31$  for a freestream wind velocity  $V_\infty = 10 \text{ m.s}^{-1}$ . Moreover, its torque coefficient  $C_\tau$  decreases linearly with the tip-speed ratio and it has a very low cut-in wind speed. These specificities make this turbine a good wind energy harvester. The geometries of the 200 mm and 100 mm runners are obtained by scaling this 300 mm rotor.

The runners have  $N = 8$  blades, a hub ratio  $H = R_H/R_T$  equal to  $H = 0.3$  and a design tip-speed ratio  $\lambda = 1$ . In the design procedure, the blade was discretized into 11 elements from the root ( $R_H$ ) to the tip ( $R_T$ ) of the blade. For each radius, a circular camber-mean line which is tangent to the relative velocity at the leading edge  $\vec{W}_1$  and at the trailing edge  $\vec{W}_2$  was drawn and thickened with NACA0010 profiles (see Fig. 1). The relative velocities at the design tip-speed ratio were predicted by applying the Euler's turbomachinery theorem and the axial momentum theory to a disc of streamtube with the hypothesis of a uniform and purely axial discharging flow  $C_1 = V_\infty(1 - a)$  with  $a = 1/3$  and a constant vortex law  $C_{\theta 2}$ . The full calculation procedure for the relative velocities can be found in Ref. [15].

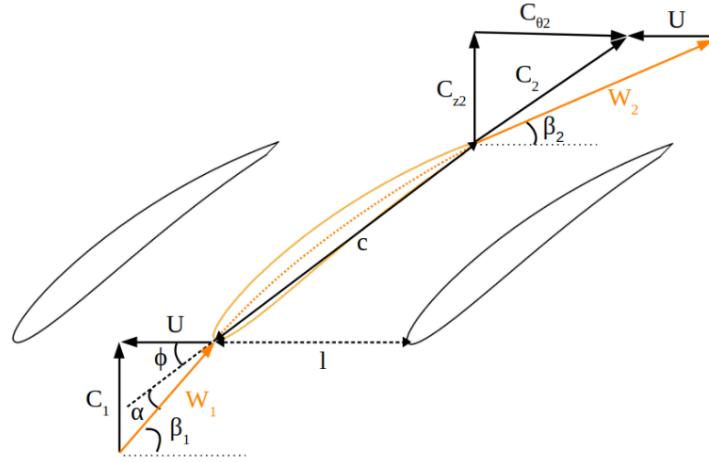


Figure 1: From Bourhis et al. [15]. Angles and velocities in blade cascade arrangement. Index 1/2 refers to the turbine's inlet/outlet.  $U$ ,  $C$  and  $W$  are the solid body rotating, absolute and relative velocities in the turbine's reference frame.  $C_\theta$  and  $C_z$  are the tangential and axial flow velocities. The blade solidity  $\sigma$  is the ratio of the blade chord length  $c$  to spacing  $l$ :  $\sigma = c/l$ .

Hub and tip chord lengths were calculated according to  $c = 2\pi r\sigma/N$  with a blade solidity at the hub  $\sigma(R_H) = 1.65$  and  $\sigma(R_T) = 0.7$  at the tip. The chord length for each radii was then determined by assuming a linear variation from hub to tip. The spanwise variations of the dimensionless chord length  $c/R_T$  and blade angles are depicted in Fig. 2. At  $\lambda = 1$ , the inlet and outlet relative angle decreases from  $\beta_1 = 66^\circ$  and  $\beta_2 = 35^\circ$  at the hub to  $\beta_1 = 34^\circ$  and  $\beta_2 = 26^\circ$  at the tip. The blade pitch angle  $\phi$ , defined as the angle between the chord line and the rotor's plane, varies from  $\phi = 55^\circ$  at the hub to  $\phi = 30^\circ$  at the tip.

Finally, the rotors were manufactured by fused material deposition with a 3D printer CREALITY CR10SPRO. The turbines were printed with polyactic acid filament and are shown in Fig. 3.

### 3. Description of the experimental setup

The aim of the experimental investigation is twofold: on one hand, to determine the power coefficient  $C_p$  and torque coefficient  $C_\tau$ , vs. tip-speed ratio  $\lambda$  characteristics for various Reynolds number by changing either the runner or the freestream wind velocity  $V_\infty$  between acquisitions and, on the other hand, to evaluate the effect of the Reynolds number on the initial wake downstream the 200 mm turbine.

#### 3.1. Power and torque coefficients measurements

The experiments were carried out in the wind tunnel of the *LIFSE* facilities. This closed-loop wind tunnel has a 1.8 m long semi-open test section with a 1.35 m×1.65 m cross-section. The turbulence ratio

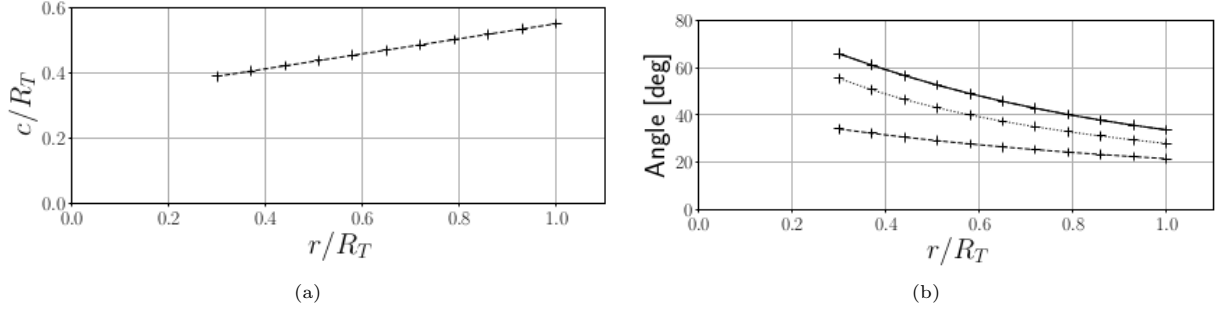


Figure 2: (a) Variations of the dimensionless chord length  $c/R_T$  according to the dimensionless radial coordinate  $r/R_T$ . (b) Variations of the inlet relative angle  $\beta_1$  (—), of the outlet relative angle  $\beta_2$  (- -) and of the pitch angle  $\phi$  (....) according to the dimensionless radial coordinate  $r/R_T$



Figure 3: Printed wind turbines used in scaling tests with a 50 euro cent coin

inside the test section is lower than 0.25%. More detailed information on the wind tunnel can be found in Refs. [21, 22]. Prior to data acquisition, the atmospheric pressure and the temperature were systematically measured to compute the daily air density. The freestream wind speed  $V_\infty$  was computed through the measurements of the dynamic pressure in the test section by a pitot transducer Furness Control FC20. The torque  $\tau$  and the angular velocity  $\omega$  were acquired using a torque transducer located between the turbine and a DC generator. These measuring devices were housed in a nacelle placed in the middle of the test section. A detailed schematic of the experimental setup is displayed in Fig. 4.

An increase in the rotor diameter or in the upcoming wind speed induces an increase in the aerodynamic torque. Therefore, in order to extend the range of measurable torque, two nacelles including torque meters with different measuring ranges were built. On one hand, the torque generated by the 300 mm runner and 200 mm runner was measured by a rotating torque meter HBM-T20WN. It has a measuring range of 0 N.m to 2 N.m and an accuracy of 0.2% of full scale. On the other hand, a second nacelle containing a rotating torque meter DRVL with a smaller measuring range was used to acquire the torque and the angular velocity of the 100 mm rotor. The latter has a measuring range of 0 N.m to 0.05 N.m and a maximum measurement error of 0.15% of full scale. The different test conditions are shown in the first two rows of Tab. 1. For each rotor, the range of upcoming wind velocity was limited by the measurement capabilities of the torque transducers.

During an acquisition, the upstream flow velocity  $V_\infty$  was kept constant while the rotational speed of the rotor  $\omega$ , *i.e.*, the operating tip-speed ratio  $\lambda$  varied between each sample by changing the resistive load applied to the generator. For each sample, the arithmetic mean value of the torque  $\tau$ , the angular velocity  $\omega$ , the temperature and the dynamic pressure in the test section were collected from 50 s long acquisitions with a sampling frequency of 1000 Hz. Then, the torque coefficient and power coefficient were computed for each sample according to the Eqs. 1&3. The experiments were repeated several times for the different set of conditions on separate days to ensure repeatability of the acquisition protocol. Finally, the data were

gathered and displayed on a single graph showing the variations of  $C_p$  and  $C_\tau$  with the tip-speed ratio for each test condition.

The Reynolds number,  $Re$ , for each experimental configurations  $\{R_T, V_\infty\}$  was calculated for analysis and is displayed in Tab. 1. The latter is computed at the hub ( $r = R_H$ ) and at the tip ( $r = R_T$ ) of the blades according to the Eq. 2 where  $W = \sqrt{(2/3V_\infty)^2 + (r\omega)^2}$ ,  $\lambda = 1$ ,  $\eta = 1.8 \cdot 10^{-5}$  Pa.s and with the arithmetic average of the air density measurements  $\rho = 1.2$  kg.m $^{-3}$ . The range of tip Reynolds numbers extend from  $Re = 22000$  (■) for the configuration  $\{50, 10\}$  to  $Re = 165200$  (×) for the configuration  $\{150, 25\}$ . As shown in Tab. 1, the 300 mm runner and 200 mm runner operate at the same Reynolds number when the upcoming wind velocity are respectively set at  $V_\infty = 10$  m.s $^{-1}$  (+) and  $V_\infty = 15$  m.s $^{-1}$  (×).

As the Reynolds number is computed with the relative velocity, a decrease in the tip-speed ratio leads to a decrease in  $Re$ . Therefore, in the following discussion, each  $\{R_T, V_\infty\}$  configuration is identified by their tip Reynolds number computed at  $\lambda = 1$  and by a specific marker in the experimental plots (see the last row of Tab. 1).

### 3.2. Test bench for near wake investigation

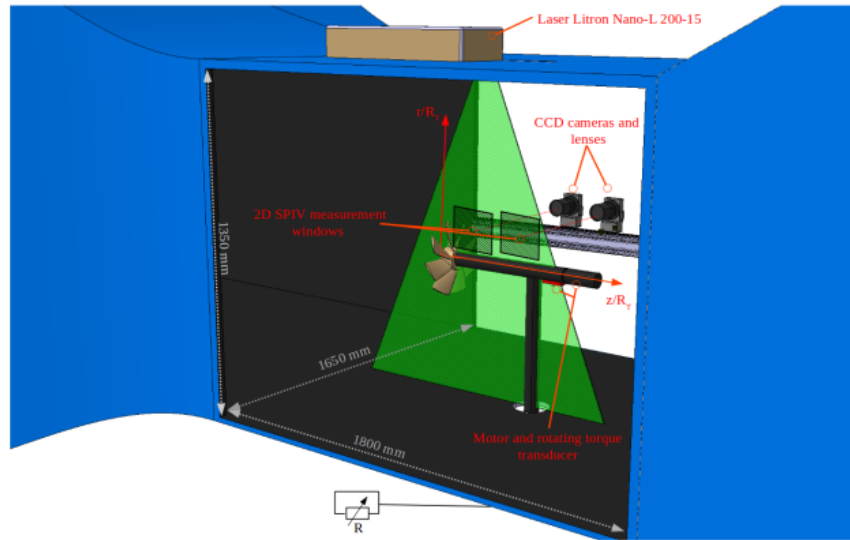


Figure 4: Detailed schematic of the closed loop wind tunnel of the *LIFSE* facilities with the experimental setup for performance measurements and 2D SPIV recordings. The two SPIV measurement windows are represented by the hashed boxes (▨) and the origin of the reference frame ( $r/R_T, z/R_T$ ) is located at the intersection of the blade leading edge and rotation axis

Phase-averaged and phase-locked 2D stereoscopic image velocimetry techniques were employed in order to evaluate the effect of the Reynolds number on the initial wake expansion and axial velocity distribution downstream the 200 mm rotor. The SPIV was performed for three freestream wind-velocity  $V_\infty = 10 - 15 - 20$  m.s $^{-1}$  with the 200 mm runners operating at its optimum tip-speed ratio  $\lambda = 1$ . The focal length of the cameras used in this study was not large enough to perform accurate SPIV analysis with the 100 mm runner. Moreover, the test section was too small to ensure that it doesn't affect wake expansion downstream the 300 mm wind turbine.

The investigation of the flow was carried out in two windows behind the 200 mm runner (please see Fig. 4). 200 and 500 double frame images were collected using two  $2048 \times 2048$  pixels CCD cameras in order to reconstruct respectively phase-locked and phase-averaged 2D velocity fields. The optical axis of the cameras were settled perpendicular to the laser sheet and focused on the oil mist droplets, used as tracer particles. Prior to acquisition, the angular velocity of the 200 mm runner was adjusted according to the freestream velocity in order to operate at  $\lambda = 1$ . The flow was illuminated twice in the observation field by a Nd:YAG, 200 mJ/pulse double pulsed Litron laser model Nano-L 200-15. The delay between the

two illuminations was chosen in order to observe a displacement of approximately 1/4 of the interrogation window for each test conditions. A pair of double frame images was captured every turn for phased-locked SPIV and every 0.5 s for phase-averaged acquisitions. After data collection, the images were divided into  $32 \times 32$  interrogation areas where the axial  $C_{z2}$  and radial  $C_{r2}$  velocity fields were reconstructed using an adaptive correlation method proposed by the software editor DANTEC. The phase-averaged and phase-locked velocity fields for each test conditions were calculated by doing the arithmetic average of  $C_{z2}$  and  $C_{r2}$  from the 500 and 200 vector velocity maps. Finally the phase-locked dimensionless vorticity fields were computed according to:

$$\omega_y \frac{c_T}{V_\infty} = \frac{c_T}{V_\infty} \left( \frac{\partial C_{r2}}{\partial z} - \frac{\partial C_{z2}}{\partial r} \right) \quad (4)$$

with  $\omega_y$  the planar vorticity and  $c_T = c(R_T)$  is the tip chord length. The intersection of the blade leading edge and the rotation axis is used as the reference frame origin.

$R_T$	[mm]	50		100		150			
$V_\infty$	[m.s <sup>-1</sup> ]	10	15	10	15	10	15	20	25
$Re(R_H)$		9500	14200	18900	28400	28400	42600	56800	71100
$Re(R_T)$		22000	33000	44100	66100	66100	99100	132200	165200
Marker in plots		■	■	+	+	×	×	×	×

Table 1: Description of the experimental test conditions  $\{R_T, V_\infty\}$ . Reynolds numbers  $Re$  are computed at the hub ( $Re(R_H)$ ) and at the tip of the blade ( $Re(R_T)$ ) according to Eq. 2. A specific marker, used to plot the experimental results, is assigned to each test condition

## 4. Results and discussions

### 4.1. Performance analysis

Fig. 5 shows the variation of the power coefficient  $C_p$  and the variation of the torque coefficient  $C_\tau$  as a function of the tip-speed ratio  $\lambda$  for the different test conditions. For all test conditions, the range of operating tip-speed ratio was limited either by the friction of the mechanical parts contain in the nacelle or by the capacity of the breaking system. No experimental power and torque coefficients were measured between  $\lambda = 0.7$  and  $\lambda = 1.1$  when the 100 mm rotor was operating at  $V_\infty = 15 \text{ m.s}^{-1}$  (■) due to a strong resonance of the transmission shaft. Furthermore, when the 300 mm runner and 200 mm runner operate at the same Reynolds number (+ & ×) both  $C_p$  and  $C_\tau$  vs.  $\lambda$  curves follow similar trends. In both test conditions, the same maximum power coefficient  $C_{p,max} = 0.31$  for an equal optimum tip-speed ratio  $\lambda_{opt} = 1$ . It emphasises that the dimension of the test section and the mechanical or electrical losses induce by the setup have no effect on the experimental measurements. The slight discrepancy in  $C_\tau$  between these two test conditions at very low tip-speed ratio might be explained by rotational effects [23] or by the difference of the blade's relative rugosity [7].

The variation of the torque coefficient with the tip-speed ratio is consistent with preliminary results reported in Ref. [15]. For all tests performed with the 300 mm runner, the torque coefficient decreases linearly for the entire range of tip-speed ratio. Even though a similar trend is observed at high tip-speed ratio with the 200 mm and 100 mm turbines, a decrease in  $Re$  leads to a change in the  $C_\tau$  vs.  $\lambda$  curves, especially at low tip-speed ratio. Nonlinear variations and a little drop in  $C_\tau$  are observed with the 200 mm and 100 mm turbines at tip-speed ratios close to  $\lambda = 0$ . A decrease in the tip-speed ratio leads to an increase in the angle of attack and a decrease in the Reynolds number. At high angles of attack, the lift curves can become highly nonlinear especially at low Reynolds number [24]. It can lead to nonlinear variations in  $C_\tau$  and  $C_p$  at low tip-speed ratios [25].

Secondly, what stands out in the Fig. 5b is the increase in  $C_\tau$  with the Reynolds number for the entire range of tip-speed ratio. At fixed  $\lambda$ , all turbines operate with the same angle of attack  $\alpha$  (see the velocity triangle in Fig. 1), hence an increase in  $Re$  leads to an increase in the net aerodynamic forces acting on the



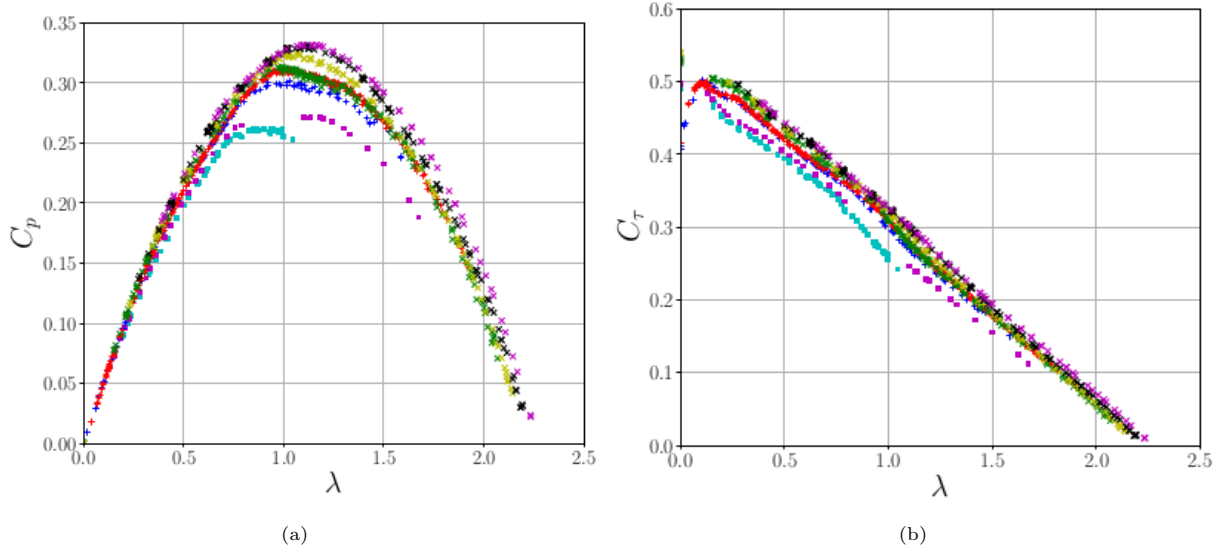


Figure 5: Power coefficient  $C_p$  (a) and torque coefficient  $C_\tau$  (b) as a function of the tip-speed ratio  $\lambda$  for various Reynolds numbers (please see the Tab. 1). The curves are obtained from the gathering of several experimental data sets for each  $\{R_T, V_\infty\}$  configuration

wind turbine's blades. Even though, this finding is directly in line with the findings on isolated airfoils, a major difference is observed between the behaviour of an isolated airfoils and a blade cascade. For isolated airfoils, an increase in the angle of attack leads to an increase in the lift coefficient until the stall angle at which a sudden decrease in the lift generated by the aerofoil occurs. Interestingly, even at low Reynolds number, no significant drop in the torque coefficient is observed while decreasing the tip-speed ratio with high-solidity blade cascade. The stall effects may be counterbalanced by the mutual interaction between the blades.

As one can see in Fig. 5a, the power coefficient  $C_p$  increases with increasing Reynolds number for the entire range of tip-speed ratio. However, a higher Reynolds number leads to narrower  $C_p$  vs.  $\lambda$  curves. These results emphasize that the  $C_l/C_d$  vs.  $\alpha$  curves of the rotating blade cascade change as the  $Re$  changes. An increase in  $Re$  induces a higher maximum  $C_l/C_d$  ratio and narrower  $C_l/C_d$  vs.  $\alpha$  curves. It implies that the aerodynamic properties of the turbine blades are more affected by a change in the angle of attack at high Reynolds number. Fig. 6a highlights the gradual increase in the maximum power coefficient  $C_{p,max}$  with the Reynolds number. For instance, the latter increases from  $C_{p,max} = 0.26$  at  $Re = 22000$  to  $C_{p,max} = 0.33$  at  $Re = 165200$ . However, the difference in  $C_{p,max}$  between each test condition decreases with  $Re$ . The trend of the  $C_{p,max}$  vs.  $\lambda$  curve suggests that the maximum power coefficient will probably level off or increases slowly. This finding is consistent with data reported on isolated airfoils [8, 26]. At high Reynolds number, the decrease in the lift coefficient and the increase in the drag coefficient of isolated airfoils are negligible. However, below a critical Reynolds number,  $C_l$  decreases fastly and  $C_d$  increases rapidly.  $C_{p,max}$  vs.  $\lambda$  curve show a very similar pattern of results. It emphasises that the effect of the Reynolds number on the maximum power coefficient occurs mainly at  $Re \leq 10^5$ .

Fig. 6b shows the variation of the optimal tip-speed ratio  $\lambda_{opt}$  with the Reynolds number. For all test conditions, the optimum tip-speed ratio is very close to the design tip-speed ratio  $\lambda = 1$ . As Figs. 5a & 6b show, there is a clear trend of increasing optimum tip-speed ratio  $\lambda_{opt}$  with the Reynolds number. Even though the  $C_l/C_d$  remains quasi-constant for  $Re \geq 10^5$ , the optimum tip-speed ratio is continuously increasing.

The variations of the dimensionless parameters with the Reynolds number may be explained by the fact that in low Reynolds number conditions  $10^4 \leq Re \leq 10^6$ , a too high adverse pressure gradient along the streamwise direction can lead to the separation of the boundary layer on the upper surface of the blades and the formation of laminar separation bubbles (LSB) inside which high recirculations of mixed laminar

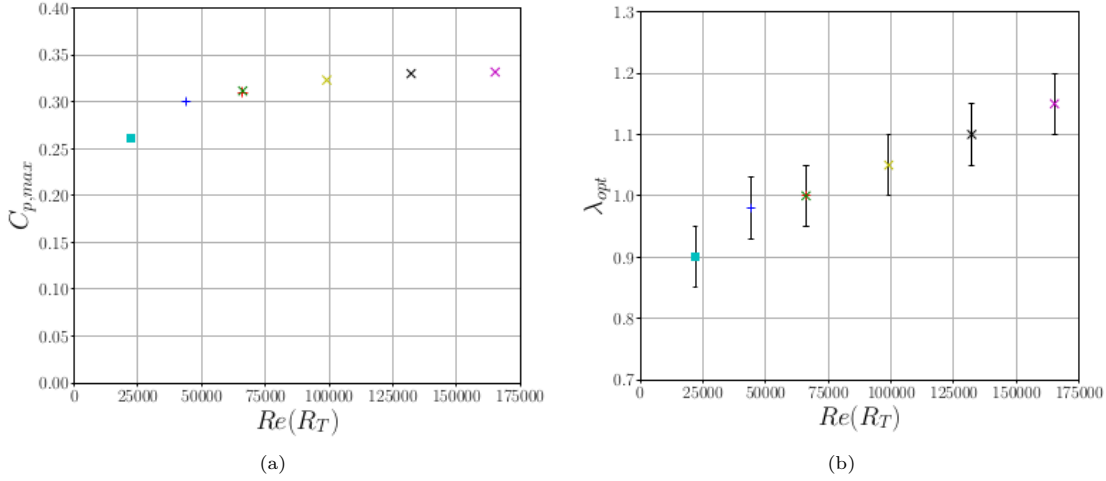


Figure 6: Effect of the Reynolds number on the maximum power coefficient  $C_{p,max}$  (a) and on the optimum tip-speed ratio  $\lambda_{opt}$  (b). The tip Reynolds number computed at  $\lambda = 1$  is used as reference for the  $Re$  axis (see Tab. 1)

and turbulent flows occur [20]. For isolated airfoils, the size of the LSB, its position on the upper surface of the blade, its separation and reattachment coordinates and its effect on the lift and drag coefficients depend on the Reynolds number, the angle of attack, the turbulence intensity and the blade's roughness [27]. With micro-scale turbines, additional phenomena are involved in the formation of LSB such as rotational effects [23] and high blade solidity effects. Our results suggest that at fixed tip-speed ratio, *i.e.*, at fixed angle of attack, the overall length and thickness of laminar separation bubbles decreases as the Reynolds number increases. Moreover, the discrepancy in the  $C_T$  vs.  $\lambda$  curves at low tip-speed ratios, *i.e.*, at very low Reynolds numbers and high angles of attack might be induced by changes in the flow regime.

#### 4.2. Near wake analysis

Phase-averaged and phase-locked stereoscopic particle image velocimetry techniques were employed for the 200 mm turbine to investigate Reynolds number effects on the initial wake. The runner was operating at the same tip-speed ratio  $\lambda = 1$  under three different flow velocity conditions:  $V_\infty = 20 \text{ m.s}^{-1}$ ,  $V_\infty = 15 \text{ m.s}^{-1}$  and  $V_\infty = 10 \text{ m.s}^{-1}$ , *i.e.*, under three tip-Reynolds number flow conditions  $Re = 88200$ ,  $Re = 66100$  and  $Re = 44100$ . An example of phase-locked and phase-averaged dimensionless axial velocity field and phase-locked dimensionless vorticity field is presented in Fig. 7.

The initial wake expansion downstream the 200 mm rotor was characterized in this study by the positions of the tip vortices shed by the turbine [6, 28]. Phase-locked SPIV vorticity fields, computed from the averaging of 200 velocity maps, were used to track the tip vortex core locations (Fig. 7c). Only the tip-vortices located before the coordinate  $z/R_T \leq 3.5$  were considered due to a variation of the nacelle geometry at  $z/R_T = 3.5$  that affects the wake. Fig. 8 shows the locations of the tip vortices in the near wake downstream the rotor for the three tested configurations. This figure highlights that the wake becomes wider with increasing Reynolds number. McTavish et al. reported a similar pattern of results on the wake expansion downstream a three bladed and low solidity turbine by performing direct flow visualization of the tip vortices in water channel [6]. In their study, the tip-Reynolds number was varied from  $Re = 3620$  to  $Re = 30100$ . The actual study demonstrates that even at larger Reynolds number, the wake expansion is still affected by the Reynolds number flow conditions. Although the range of Reynolds number is significantly lower than in the case of full-scale turbines, our results demonstrate that the effect of the upstream wind velocity wake expansion downstream a rotor should be taken into account in the design of wind farms, for example. As the wake becomes wider with the Reynolds number, it could conceivably be hypothesised that full-scale turbines's wake present large wake that could affect the operating conditions of near turbines.

The effect of the Reynolds number on the averaged axial flow velocity defect was also evaluated. The

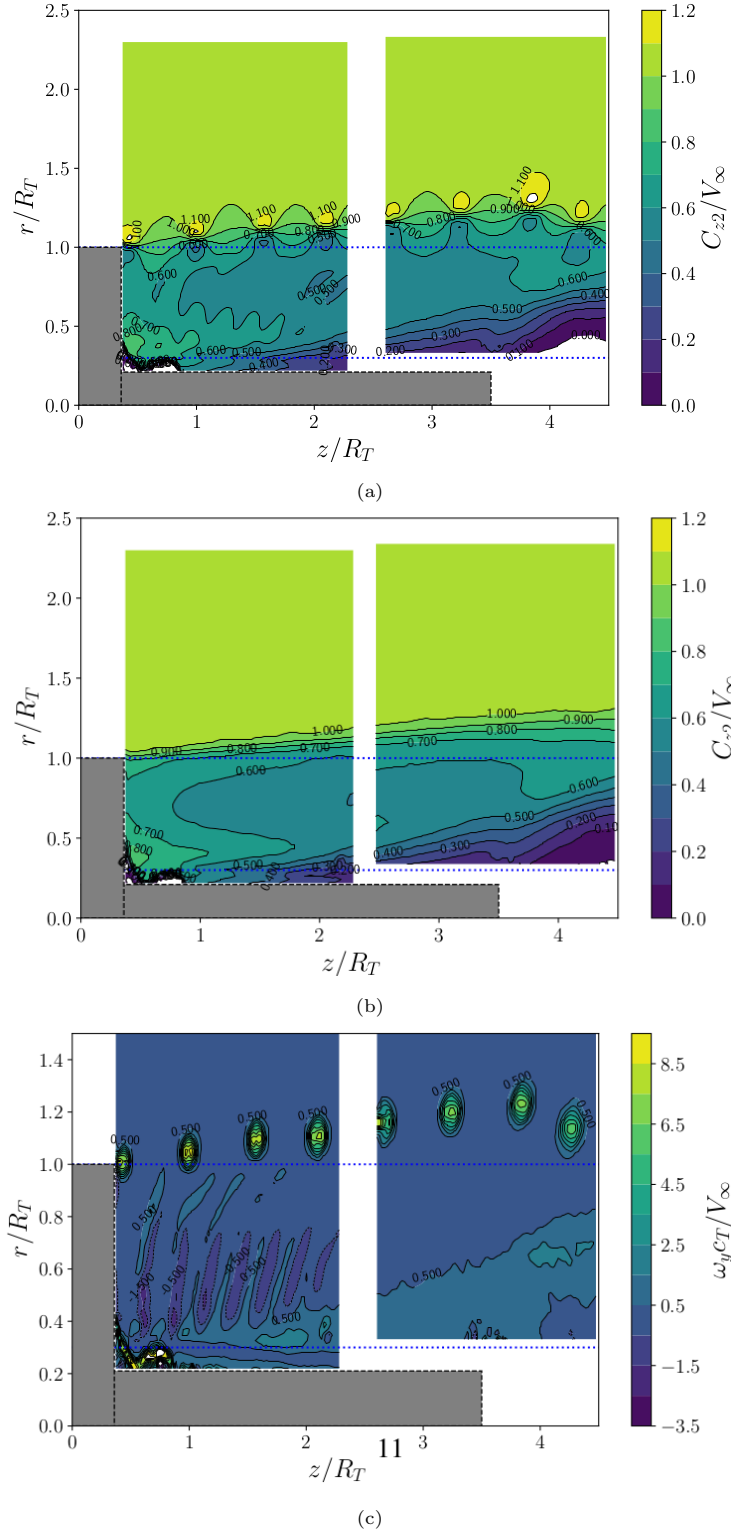


Figure 7: Phase-locked (a) and phase-averaged (b) dimensionless axial velocity fields  $C_{z2}/V_\infty$ . Phase-locked dimensionless vorticity field  $c_T \omega_y/V_\infty$  (c). The fields are computed from SPIV acquisitions for the 200 mm runner operating at  $V_\infty = 20 \text{ m.s}^{-1}$  and  $\lambda = 1$

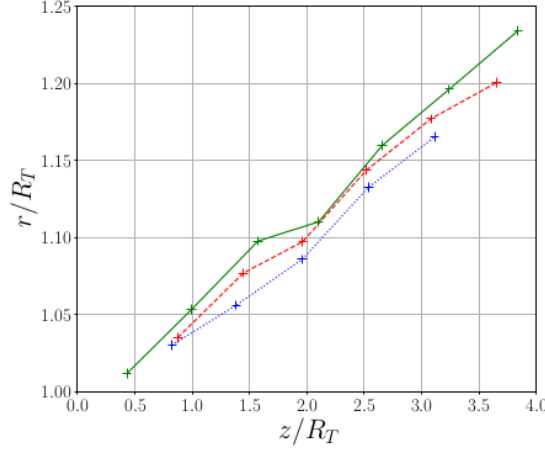


Figure 8: Effect of the Reynolds number on the initial wake expansion for the 200 mm runner operating at  $\lambda = 1$  and at  $V_\infty = 20 \text{ m.s}^{-1}$  (—),  $V_\infty = 15 \text{ m.s}^{-1}$  (- -) and  $V_\infty = 10 \text{ m.s}^{-1}$  (····). The lines joining the mean vortex core locations have been added for a more convenience data visualisation

dimensionless phase-averaged axial velocity profiles for various horizontal coordinate were derived from the phase-averaged acquisitions (Fig. 7b). One interesting finding is that an increase in the Reynolds number leads to a decrease in the near wake dimensionless axial velocity  $C_{z2}/V_\infty$  (Fig. 9). This pattern was observed for various horizontal distance from the blade leading edge:  $z/R_T = 1$  (—),  $z/R_T = 2$  (- -) and  $z/R_T = 2$  (····). The larger velocity defect in the near wake in high Reynolds number flow conditions corroborates the increase in the maximum power coefficient with the Reynolds number presented in § 4.1. What stands out in this figure is that the main differences in  $C_{z2}/V_\infty$  are observed in the inner part of the blade, whereas the  $C_{z2}/V_\infty$  vs.  $r/R_T$  curves are close to each other in the outer part of the blade. Even though the range of examined Reynolds number remains limited, our results emphasised that the near wake downstream the 200 mm turbine is strongly dependent on the Reynolds number. Thus, both wake expansion and deceleration should be corrected in wind tunnel tests of scaled turbines in order to provide relevant insights for the design of efficient wind farms.

Furthermore, Reynolds number effects should also be taken into account in the design of an efficient wind energy harvester, especially in the choice of a specific airfoil. Airfoil polar plots are obtained in wind tunnel for a specific Reynolds number. At high Reynolds number ( $Re \geq 10^6$ ), the lift and drag coefficients vs. angle of attack curves are practically independent of the Reynolds number [8]. Large-scale wind turbines operate at large and quasi-constant Reynolds number, hence it is not crucial in the blade's design to take into account the effect of the Reynolds number on the aerodynamic properties of the airfoil. On the contrary, for micro-scale wind turbine, the Reynolds number varies strongly from the hub to the tip of the blade due to either the spanwise variation of the rotating speed  $U = r\omega$  or due to a variation of the operating freestream wind velocity  $V_\infty$  (see Tab. 1). The flow regime along the span can differ greatly from a laminar regime close to the hub to a transient or turbulent regime at the tip. Hence, instead of choosing an airfoil based on the maximum lift to drag ratio at a fixed Reynolds number, it could be preferable to select an airfoil that doesn't present high variability of its aerodynamic properties for the Reynolds number entire range of operation.

## 5. Conclusion

The current study sought to investigate the effects of the Reynolds number on the  $C_\tau$  and  $C_p$  vs.  $\lambda$  curves of high-solidity micro-scale wind turbines, as well as the effects on the near wake characteristics. Three geometrically scaled high-solidity and low tip-speed ratio wind turbines with rotor diameters equal to 300 mm, 200 mm, and 100 mm were designed based on Euler's turbomachinery theorem, manufactured

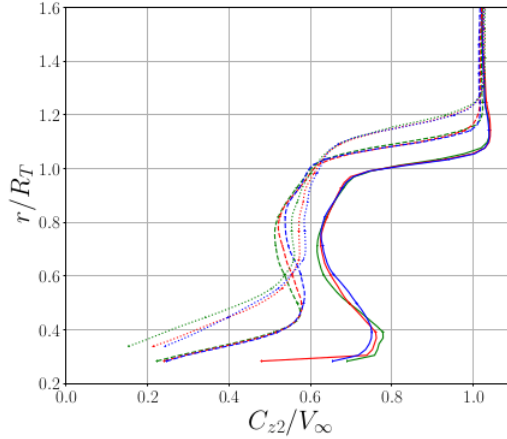


Figure 9: Effect of the Reynolds number on the dimensionless axial velocity profiles  $C_{z2}/V_{\infty}$  for various dimensionless horizontal distance from the blade leading edge:  $z/R_T = 1$  (—),  $z/R_T = 2$  (---),  $z/R_T = 3$  (····). The 200 mm runner was operating at  $\lambda = 1$  and at  $V_{\infty} = 20 \text{ m.s}^{-1}$  (shown in green),  $V_{\infty} = 15 \text{ m.s}^{-1}$  (shown in red) and  $V_{\infty} = 10 \text{ m.s}^{-1}$  (shown in blue)

by fused material deposition, and tested in a wind tunnel under various freestream wind velocities. The research has identified that an increase in the Reynolds number from  $Re = 22000$  to  $Re = 165200$  leads to an increase in the maximum power coefficient from  $C_{p,max} = 0.26$  to  $C_{p,max} = 0.33$ . However,  $C_{p,max}$  remains nearly constant for  $Re \geq 10^5$ . The second major finding was that higher Reynolds number flow conditions lead to higher torque coefficients  $C_{\tau}$  and power coefficients  $C_p$  for the entire range of tip-speed ratios. The experiments have shown that the optimum tip-speed ratio, *i.e.*, the optimum angle of attack of the blade cascade increases, as the Reynolds number increases. Finally, the analysis of the near wake of the 200 mm turbine for three upcoming wind velocities has shown that a larger operating Reynolds number leads to wider wake expansion and a larger axial velocity defect. As a result, wind tunnel experiments with micro-scale turbines are useful to get relevant insights on the performance and wake of a turbine. However, the decrease in Reynolds number due to scaled experiments leads to a change in flow regime and in the performance of a runner. Thus, faithful scaled experiments should be performed by either changing the geometry of the rotor and the airfoil to match the wake and performances of large-scale turbines [6] or by correcting the data obtained from scaled experiments [29]. Even though this current study provides quantitative experimental data that strengthens the idea that the wake and performance of micro-scale turbines are strongly affected by the Reynolds number, further investigations are needed to fully understand its implications on the flow pattern around wind turbines' blades. A wider range of Reynolds numbers and an investigation of the third component of the flow velocity by SPIV would be of particular great interest to either design more efficient wind energy harvesters or to examine closely the scaling effects of large turbines.

## References

- [1] Xi Lu, Michael B. McElroy, and Juha Kiviluoma. Global potential for wind-generated electricity. *Proceedings of the National Academy of Sciences*, 106(27):10933–10938, 2009.
- [2] Samira Keivanpour, Amar Ramudhin, and Daoud Ait Kadi. The sustainable worldwide offshore wind energy potential: A systematic review. *Journal of Renewable and Sustainable Energy*, 9(6):065902, 2017.
- [3] Andrey Somov and Raffaele Giaffreda. Powering iot devices: Technologies and opportunities. *IEEE IoT Newsletter*, 2015.
- [4] Quan Wen, Xianming He, Zhuang Lu, Reinhard Streiter, and Thomas Otto. A comprehensive review of miniaturized wind energy harvesters. *Nano Materials Science*, 3(2):170–185, 2021. Nano Energy Materials and Devices for Miniaturized Electronics and Smart Systems.
- [5] Ali M. Eltamaly, Majed A. Alotaibi, Abdulrahman I. Alolah, and Mohamed A. Ahmed. Iot-based hybrid renewable energy system for smart campus. *Sustainability*, 13(15), 2021.
- [6] S. McTavish, Daniel Feszty, and F. Nitzsche. Evaluating reynolds number effects in small-scale wind turbine experiments. *Journal of Wind Engineering and Industrial Aerodynamics*, 120:81–90, 09 2013.
- [7] Timothy Burdett and Kenneth Van Treuren. Scaling small-scale wind turbines for wind tunnel testing. volume 6, 06 2012.

- [8] John Cunningham and Patrick Lemieux. *Study of Low Reynolds Number Effects on Small Wind Turbine Performance*.
- [9] Damian Kadrowski, Michal Kulak, Michal Lipian, Malgorzata Stepień, Piotr Baszczynski, Karol Zawadzki, and Maciej Karczewski. Challenging low reynolds - swt blade aerodynamics. *MATEC Web of Conferences*, 234:01004, 01 2018.
- [10] Stefania Zanforlin and Stefano Deluca. Effects of the reynolds number and the tip losses on the optimal aspect ratio of straight-bladed vertical axis wind turbines. *Energy*, 148:179–195, 2018.
- [11] Gaohua Li, Wenhao Xu, Ye Li, and Fuxin Wang. Univariate analysis of scaling effects on the aerodynamics of vertical axis wind turbines based on high-resolution numerical simulations: The reynolds number effects. *Journal of Wind Engineering and Industrial Aerodynamics*, 223:104938, 2022.
- [12] JN. Sørensen. *General Momentum Theory for Horizontal Axis Wind Turbines*, volume 4 of *Research Topics in Wind Energy*. Springer International Publishing, Cham, 2016.
- [13] Justin Winslow, Hikaru Otsuka, Bharath Govindarajan, and Inderjit Chopra. Basic understanding of airfoil characteristics at low reynolds numbers (104–105). *Journal of Aircraft*, 55(3):1050–1061, 2018.
- [14] Kenneth W. Van Treuren. Small-scale wind turbine testing in wind tunnels under low reynolds number conditions. *Journal of Energy Resources Technology*, 137(5), 09 2015.
- [15] M. Bourhis, M. Pereira, F. Ravelet, and I. Dobrev. Innovative design method and experimental investigation of a small-scale and very low tip-speed ratio wind turbine. *Experimental Thermal and Fluid Science*, 130:110504, 2022.
- [16] Dennis Leung, Y. Deng, and Michael K.H. Leung. Design optimization of a cost-effective micro wind turbine. *WCE 2010 - World Congress on Engineering 2010*, 2:988–993, 2010.
- [17] Matthew M. Duquette, Jessica Swanson, and Kenneth D. Visser. Solidity and Blade Number Effects on a Fixed Pitch, 50 W Horizontal Axis Wind Turbine. *Wind Engineering*, 27(4):299–316, 2003.
- [18] Karol Zawadzki, Wojciech Smiechowicz, Malgorzata Stepień, Anna Baszcznska, and Michal Tarkowski. Influence of the Solidity Ratio on the Small Wind Turbine Aerodynamics. *E3S Web of Conferences*, 242:03006, January 2021.
- [19] D. J. Sharpe. A general momentum theory applied to an energy-extracting actuator disc. *Wind Energy*, 7(3):177–188, 2004.
- [20] P B S Lissaman. Low-Reynolds-Number Airfoils. *Annual Review of Fluid Mechanics*, 15(1):223–239, 1983.
- [21] M. Bourhis, M. Pereira, and F. Ravelet. Experimental investigation of the effect of blade solidity on micro-scale and low tip-speed ratio wind turbines. *Experimental Thermal and Fluid Science*, 140:110745, 2023.
- [22] Ivan Dobrev and Fawaz Massouh. Cfd and piv investigation of unsteady flow through savonius wind turbine. *Energy Procedia*, 6:711–720, 2011.
- [23] H. Himmelskamp, Aerodynamische Versuchsanstalt Göttingen, Great Britain. Ministry of Aircraft Production, and Luftfahrtforschungsanstalt Hermann Georing. *Profile Investigations on a Rotating Airscrew*. ARC-10856. Ministry of Aircraft Production, 1947.
- [24] S Worasinchai, G Ingram, and R Dominy. A low-reynolds-number, high-angle-of-attack investigation of wind turbine aerofoils. *Proceedings of the Institution of Mechanical Engineers, Part A: Journal of Power and Energy*, 225(6):748–763, 2011.
- [25] Hakjin Lee and Duck-Joo Lee. Low reynolds number effects on aerodynamic loads of a small scale wind turbine. *Renewable Energy*, 154:1283–1293, 2020.
- [26] Shubham Jain, Nekkanti Sitaram, and Sriram Krishnaswamy. Effect of reynolds number on aerodynamics of airfoil with gurney flap. *International Journal of Rotating Machinery*, 2015, 09 2015.
- [27] Tianyu Xia, Hao Dong, Liming Yang, Shicheng Liu, and Zhou Jin. Investigation on flow structure and aerodynamic characteristics over an airfoil at low reynolds number—a review. *AIP Advances*, 11(5):050701, 2021.
- [28] R. Soto-Valle, S. Cioni, S. Bartholomay, M. Manolesos, C. N. Nayeri, A. Bianchini, and C. O. Paschereit. Vortex identification methods applied to wind turbine tip vortices. *Wind Energy Science*, 7(2):585–602, 2022.
- [29] Marianela Machuca Macias, Rafael Mendes, Taygoara Oliveira, and Antonio Brasil Junior. On the upscaling approach to wind tunnel experiments of horizontal axis hydrokinetic turbines. *Journal of the Brazilian Society of Mechanical Sciences and Engineering*, 42, 09 2020.